Science Robotics
AAAS

robotics.sciencemag.org/cgi/content/full/5/41/eaaz7946/DC1

Supplementary Materials for

Biofuel-powered soft electronic skin with multiplexed and wireless sensing for human-machine interfaces

You Yu, Joanna Nassar, Changhao Xu, Jihong Min, Yiran Yang, Adam Dai, Rohan Doshi, Adrian Huang, Yu Song, Rachel Gehlhar, Aaron D. Ames, Wei Gao*

*Corresponding author. Email: weigao@caltech.edu

Published 22 April 2020, *Sci. Robot.* **5**, eaaz7946 (2019)
DOI: 10.1126/scirobotics.aaz7946

The PDF file includes:

Other Supplementary Material for this manuscript includes the following:

(available at robotics.sciencemag.org/cgi/content/full/5/41/eaaz7946/DC1)

Movie S1 (.mp4 format). Biofuel-powered electronic skin for robotic arm control and cargo handling.
Movie S2 (.mp4 format). Biofuel-powered electronic skin for prosthesis control.

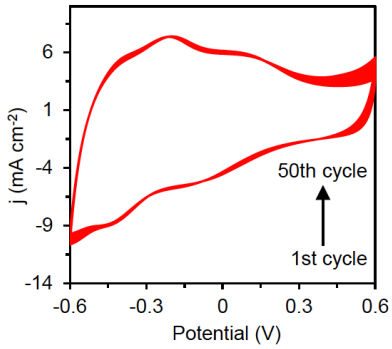

Fig. S1. CVs of an MDB-CNT/rGO/h-Ni electrode. Scan rate, 50 mV s^{-1}.

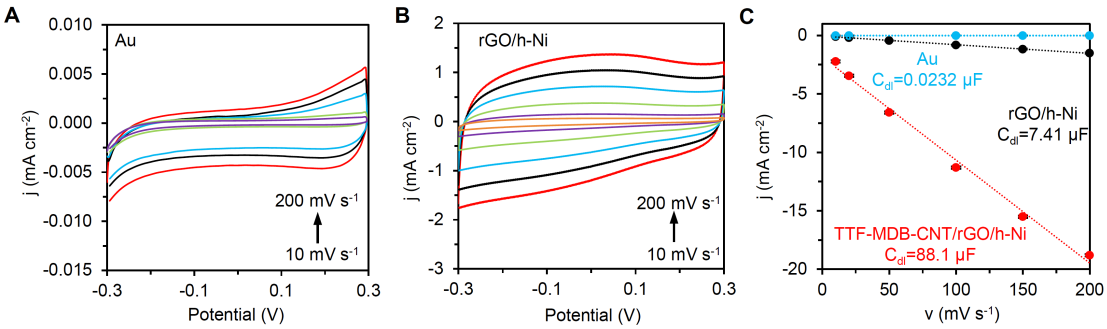

Fig. S2. Characterization of the surface area of the BFC anodes. (**A** and **B**) CVs of a Au electrode (**A**) and an rGO/h-Ni electrode (**B**). Scan rate range:10 mV s^{-1}–200 mV s^{-1}. (**C**) Current densities of the Au, rGO/h-Ni, and TTF-MDB-CNT/rGO/h-Ni electrodes at -0.1 V plotted against scan rate (v). Error bars represent the SDs from five scan cycles. C_{dl}, the double-layer capacitance per square centimeter. C_{dl} is calculated as the slope of the linear fitting.

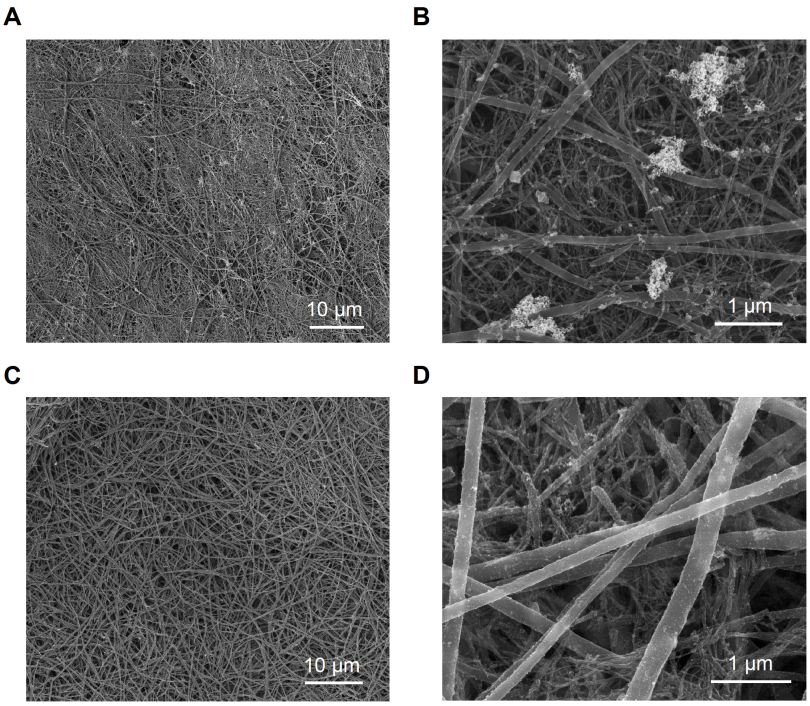

Fig. S3. Role of MDB in the preparation of the Pt/CNT BFC cathodes. SEM images of the Pt/CNT (**A** and **B**) and Pt/MDB-CNT (**C** and **D**) electrodes.

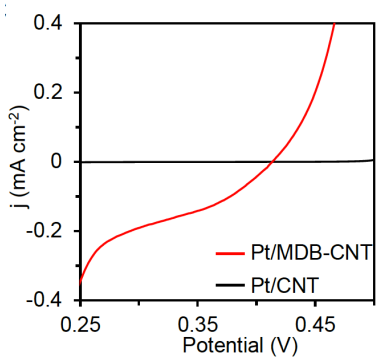

Fig. S4. Characterization of the Pt/CNT and the Pt/MDB-CNT cathodes. The linear sweeping voltammograms (LSVs) suggest high performance of the Pt/MDB-CNT electrode for O_2 reduction. Experiments were repeated three times independently with similar results.

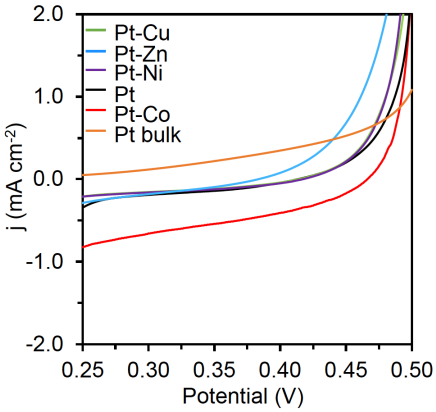

Fig. S5. Characterization of the bulk Pt, Pt/MDB-CNT, and Pt alloy/MDB-CNT cathodes. Linear sweeping voltammograms (LSVs) of bulk Pt electrode, Pt/MDB-CNT, Pt-M/MDB-CNT (M=Co, Ni, Zn, or Cu). Scan rate, 5 mV s^{-1}. Experiments were repeated three times independently with similar results.

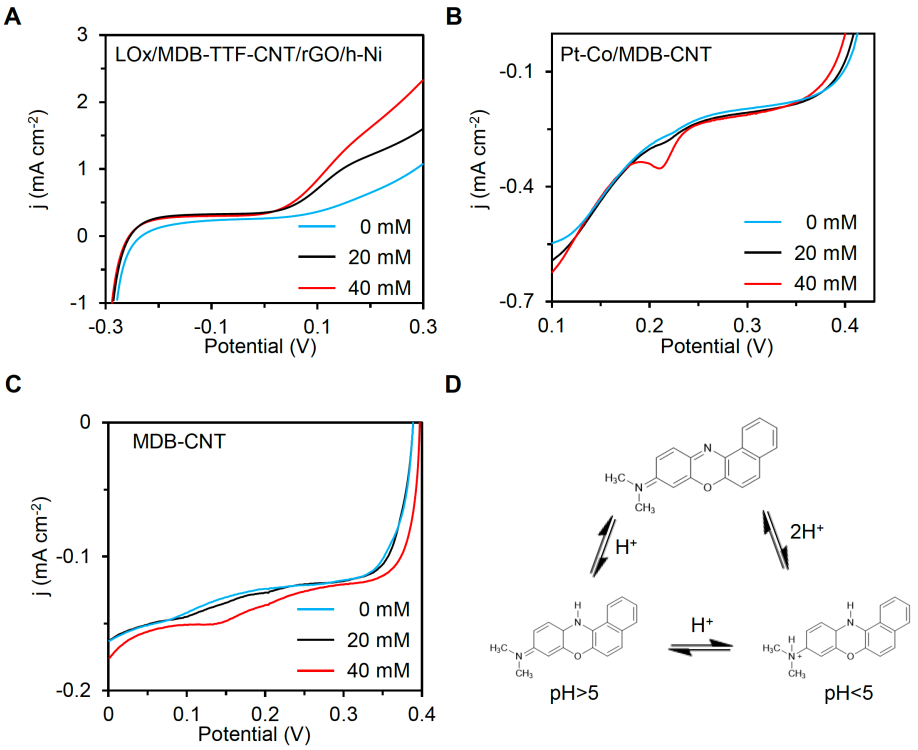

Fig. S6. LSV characterization of the bioanode and the cathodes in lactate solutions. (**A** to **C**) LSVs of the LOx/TTF-MDB-CNT/rGO/h-Ni (**A**), Pt-Co/MDB-CNT (**B**), and MDB-CNT (**C**) electrodes in 0, 20 and 40 mM lactate solutions. Scan rate, 5 mV s^{-1}. (**D**) The forms of the MDB under different pHs. Experiments were repeated three times independently with similar results.

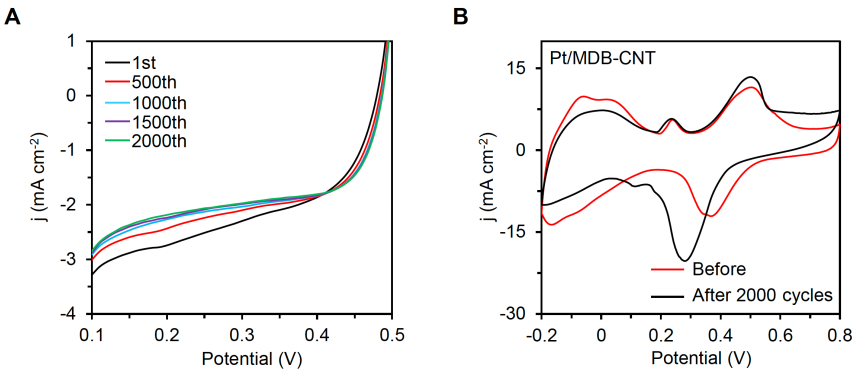

Fig. S7. Characterization of the stability of the Pt/MDB-CNT cathode. (**A**) Repetitive LSVs of a Pt/MDB-CNT cathode for over 2000 cycles. Current density of the Pt/MDB-CNT cathode shows significant decrease over time. (**B**) CVs of a Pt/MDB-CNT cathode before and after 2000 cycles catalysis recorded in N_2-purged 0.1 M H_2SO_4 solutions. Scan rate, 100 mV s^{-1}. The ECSA of the cathode, characterized by the adsorption/desorption of hydrogen on Pt (integral area in the range of -0.2 to 0.1 V), decreases significantly after 2000 cycles. Experiments were repeated three times independently with similar results.

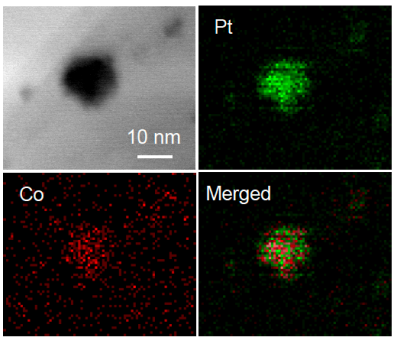

Fig. S8. Characterization of the Pt-Co alloy nanoparticles. Scanning transmission electron microscope (STEM) image of a Pt-Co alloy nanoparticle and the corresponding elemental mappings of Pt and Co.

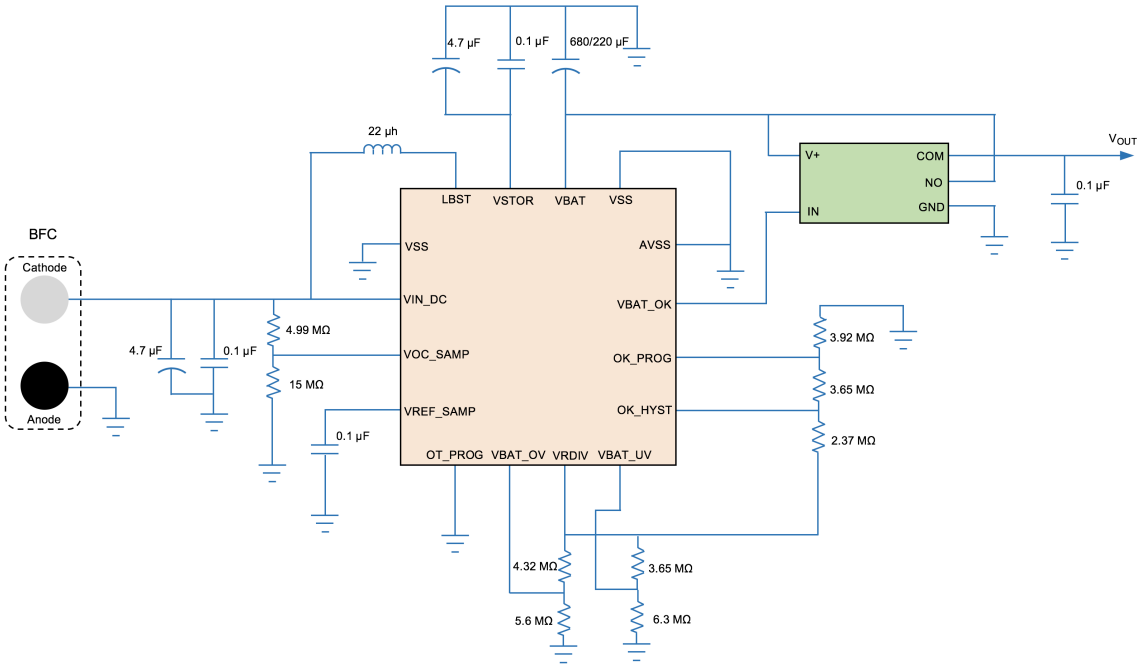

Fig. S9. Schematic diagram of the energy-harvesting circuit.

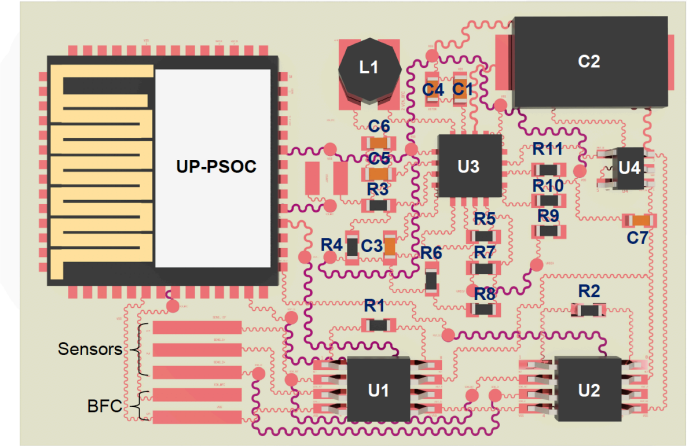

The list of the components.

Components	Description	Value and series number
UP-PSOC	EZ-BLE™ Creator Module	CYBLE-214009-00
U1	Instrumentation Amplifier	INA 333
U2	Instrumentation Amplifier	INA 333
U3	Boost Converter	BQ25504
U4	Analogue Switch	MAX4715EXK+T
L1	Fixed Inductors	WE-TPC 2828
C1	0402 Capacitor	4.7 μF
C2	Tantalum Capacitors	680 μF
C3	0402 Capacitor	0.01 μF
C4	0402 Capacitor	0.1 μF
C5	0402 Capacitor	4.7 μF
C6	0402 Capacitor	0.1 μF
C7	0402 Capacitor	0.1 μF
R1	0402 Resistor	∞
R2	0402 Resistor	∞
R3	0402 Resistor	4.99 MΩ
R4	0402 Resistor	15 MΩ
R5	0402 Resistor	4.32 MΩ
R6	0402 Resistor	5.6 MΩ
R7	0402 Resistor	3.65 MΩ
R8	0402 Resistor	6.2 MΩ
R9	0402 Resistor	2.37 MΩ
R10	0402 Resistor	3.65 MΩ
R11	0402 Resistor	3.92 MΩ

Fig. S10. Schematic illustration and component list of the electronic system of the PPES. R1 and R2 are the gain resistors (Rg). The gain G=1+(100kΩ/Rg).

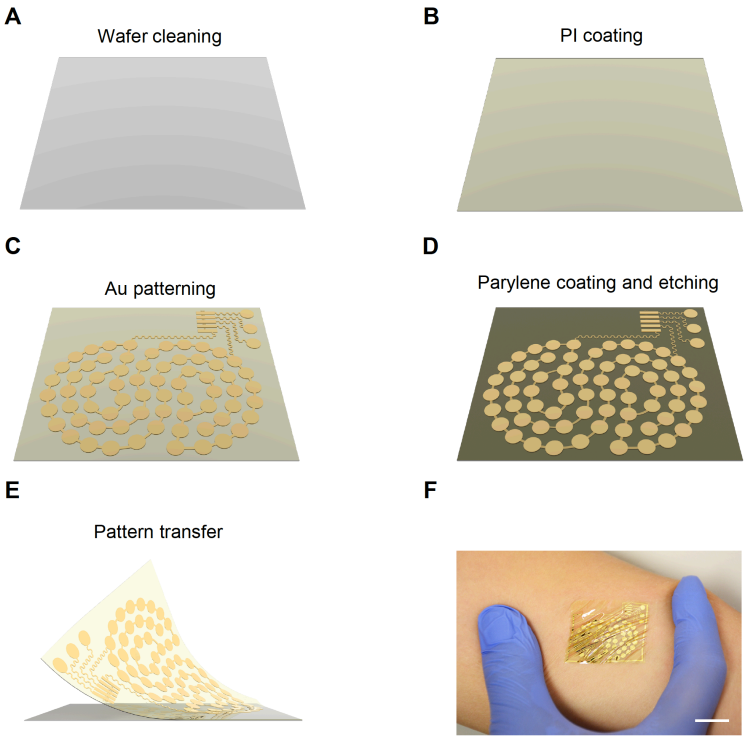

Fig. S11. Fabrication process of the electrochemical patch of the PPES. (**A**) Wafer cleaning. (**B**) Spin-coating of PI (9 μm) on the handling wafer. (**C**) Electrode patterning using photolithography, electron-beam evaporation and lift-off in acetone. (**D**) Parylene insulating layer patterning. (**E**) BFC-sensor patch release from the wafer. (**F**) Photograph of a soft electrochemical BFC-sensor patch on the skin. Scale bar, 2 cm.

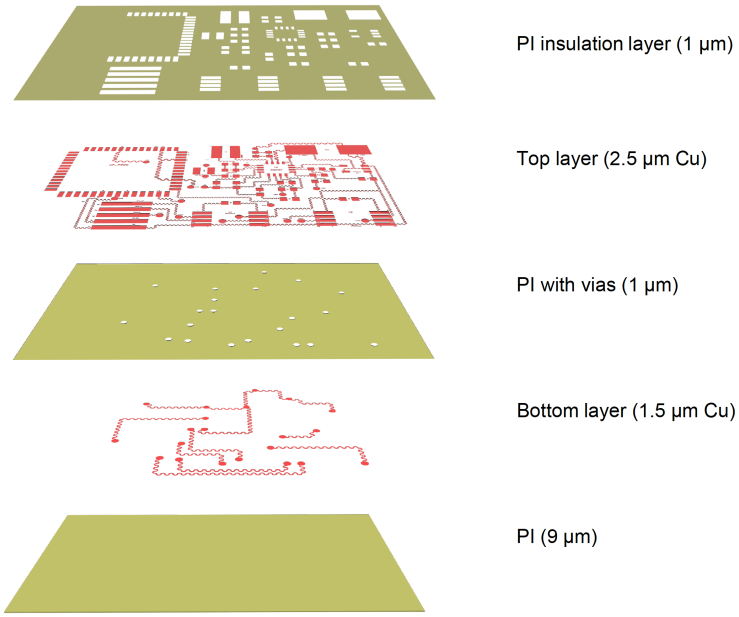

Fig. S12. Exploded view of the multilayered electronic patch.

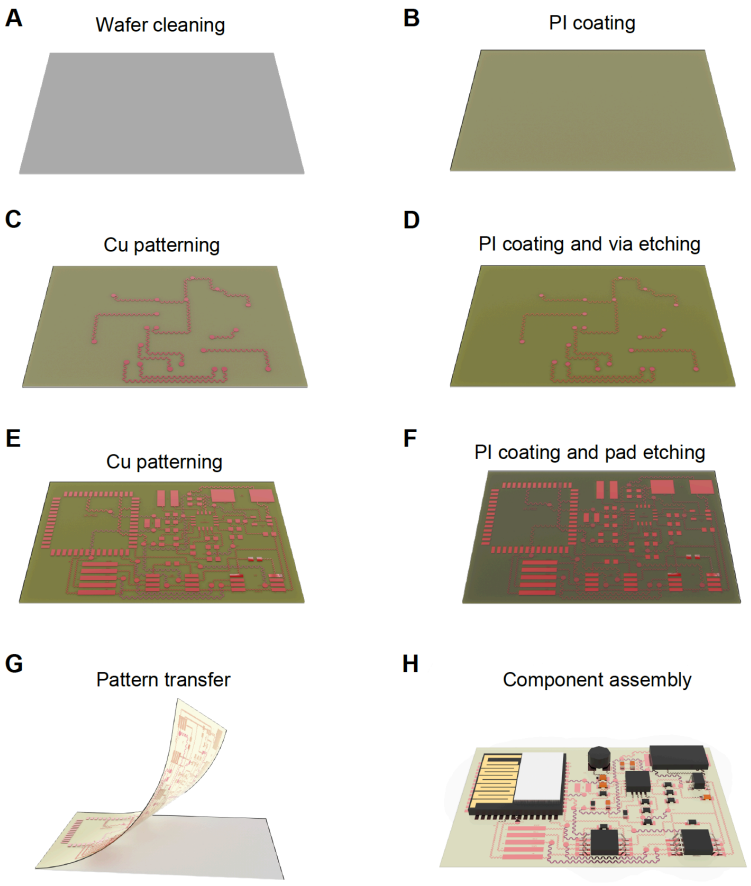

Fig. S13. Fabrication process of the flexible electronic patch of the PPES. (**A**) Wafer cleaning. (**B**) Spin-coating of PI (9 μm) on the handling wafer. (**C**) Cu patterning (1.5 μm) using photolithography, electron-beam evaporation, and lift-off. (**D**) Insulating PI layer (1 μm) coating and via etching. (**E**) Cu patterning using photolithography, electron-beam evaporation (2.5 μm) and lift-off in acetone. (**F**) Insulating PI layer (1 μm) coating and selective etching of the connecting pads. (**G**) Patch release from the wafer. (**H**) Assembling of the electronic components on the soft electronic patch.

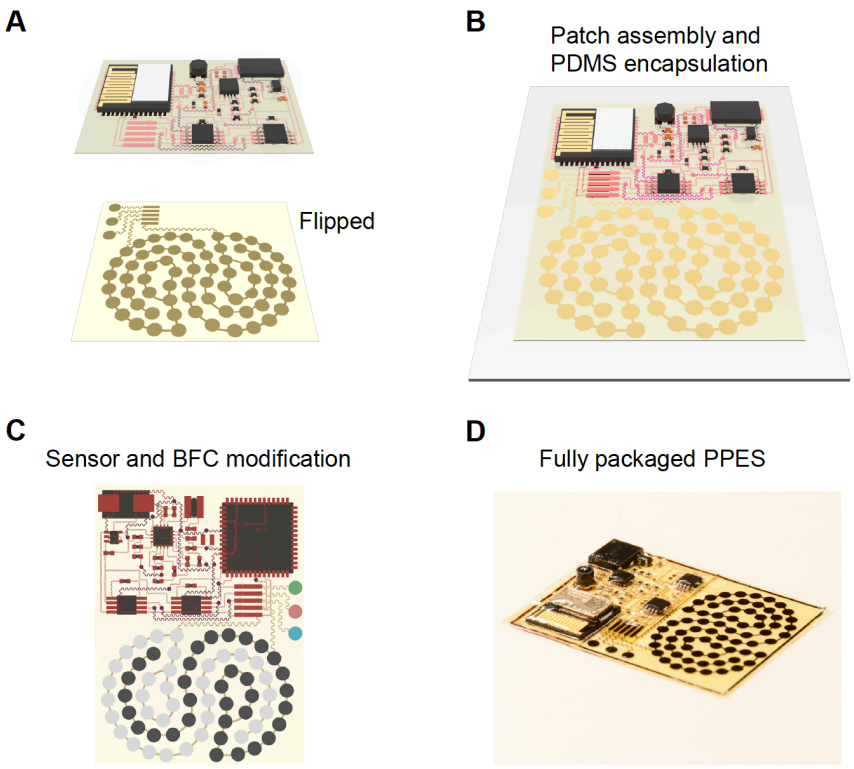

Fig. S14. Assembly and encapsulation of the PPES. (**A**) The flipped electrochemical and the electronic patches. (**B**) The flipped electrochemical patch and electronic patch are connected with the conductive paste and encapsulated with PDMS. (**C**) The sensor array is modified with urea/NH_4^+ or glucose/pH sensing films and the BFC electrodes are assembled on the PPES. (**D**) Photograph of a fully packaged PPES.

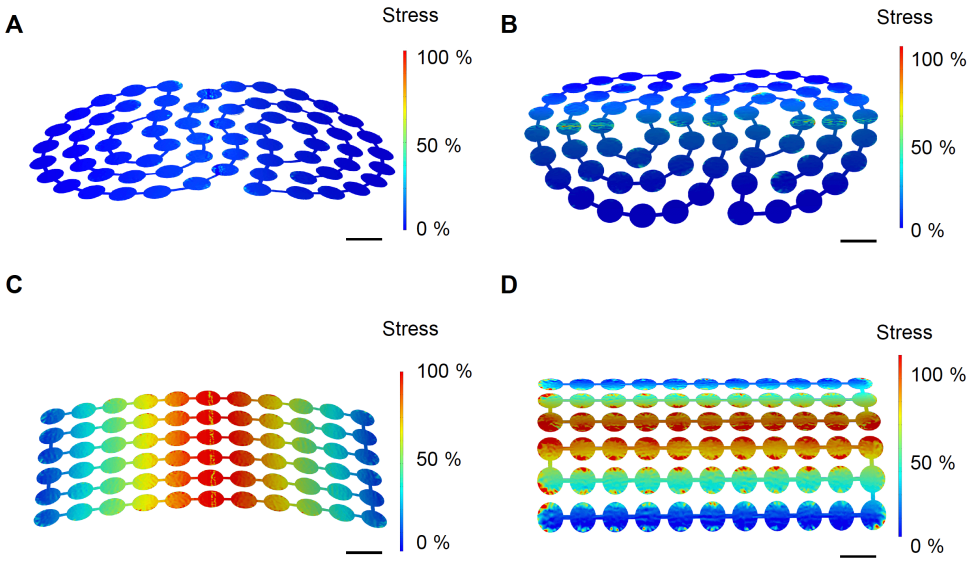

Fig. S15. Mechanical deformation study of the BFC patch. Numerical simulation of stress distributions of the BFC array with serpentine design (**A** and **B**) and the straight-line design (**C** and **D**) under mechanical deformation (0.05% strains). Scale bars, 3 mm.

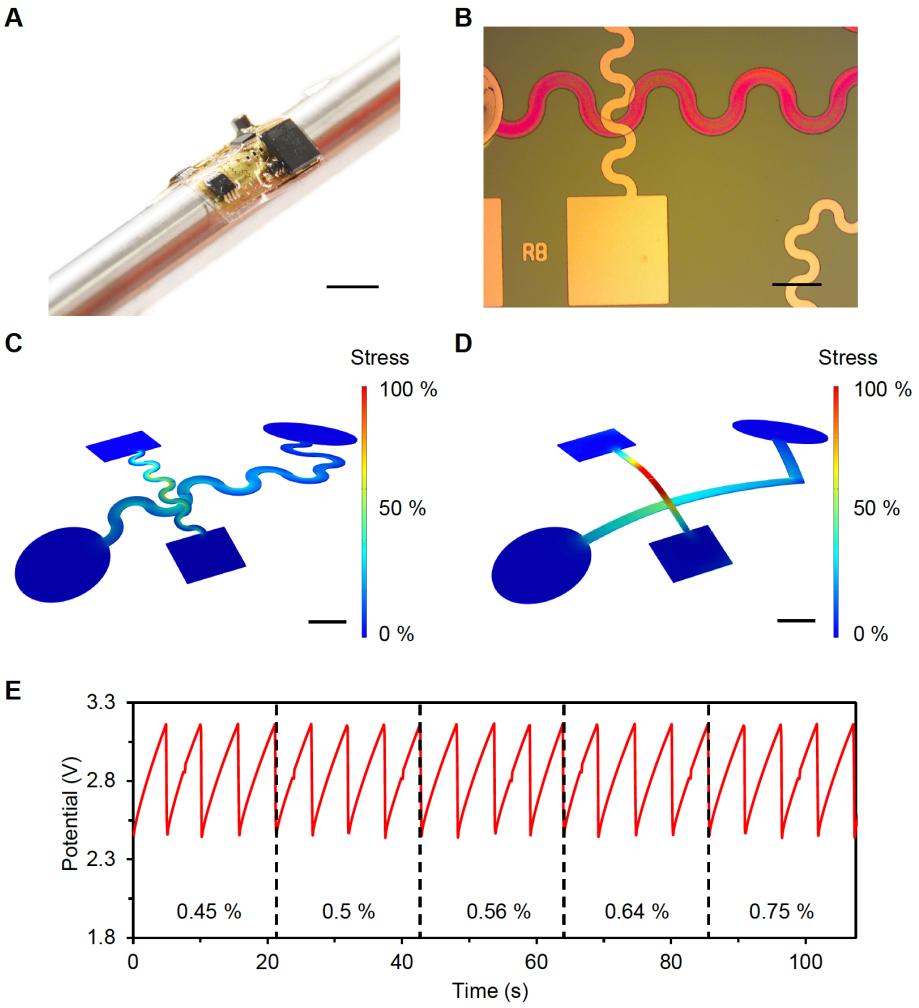

Fig. S16. Mechanical deformation study of the electronic patch. (**A**) Photograph of a soft electronic patch of the PPES under mechanical deformation. Scale bar, 1 cm. (**B**) Photograph of typical interconnect patterns on the electronic patch. (**C** and **D**) Numerical simulation of stress distributions of the wavy cross structure (**C**) and the straight line structure (**D**) under mechanical deformation (0.05% strain). Scale bars, 0.3 mm. (**E**) Dynamics of the capacitor potential under strains between 0.45 % and 0.75 % with constant power supply (input signal, 0.5 V and 2 mA).

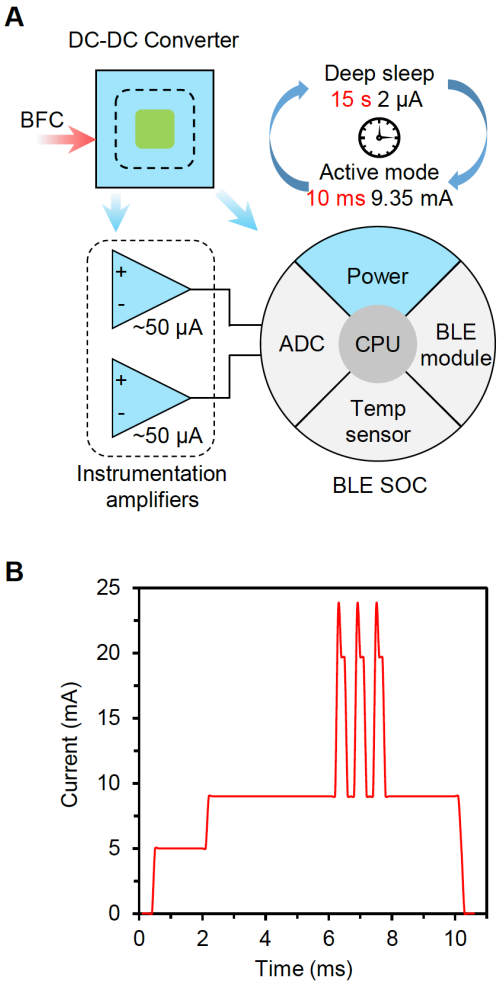

Fig. S17. Power consumption breakdown of the PPES. (A) Power consumption of the PPES. (**B**) Power consumption of the PSoC module during the wake-up operation. Operation potential, 3.3 V.

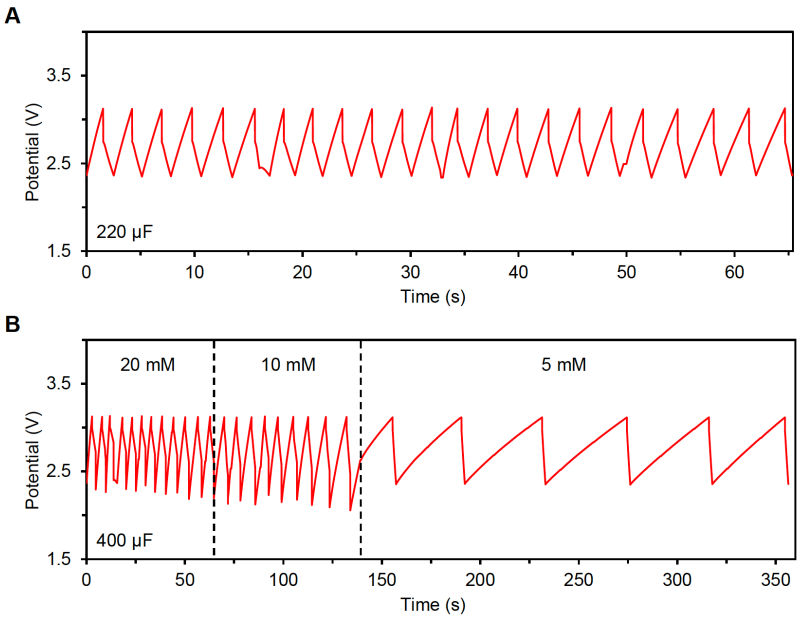

Fig. S18. Continuous operation of the PPES with small capacitors in 5 to 20 mM lactate. (**A**) Real-time capacitor potential of the PPES measured during continuous operation in 20 mM lactate. Capacitor, 220 µF. (**B**) Real-time capacitor potential of the PPES measured during continuous operation in 20, 10, and 5 mM lactate. Capacitor, 400 µF.

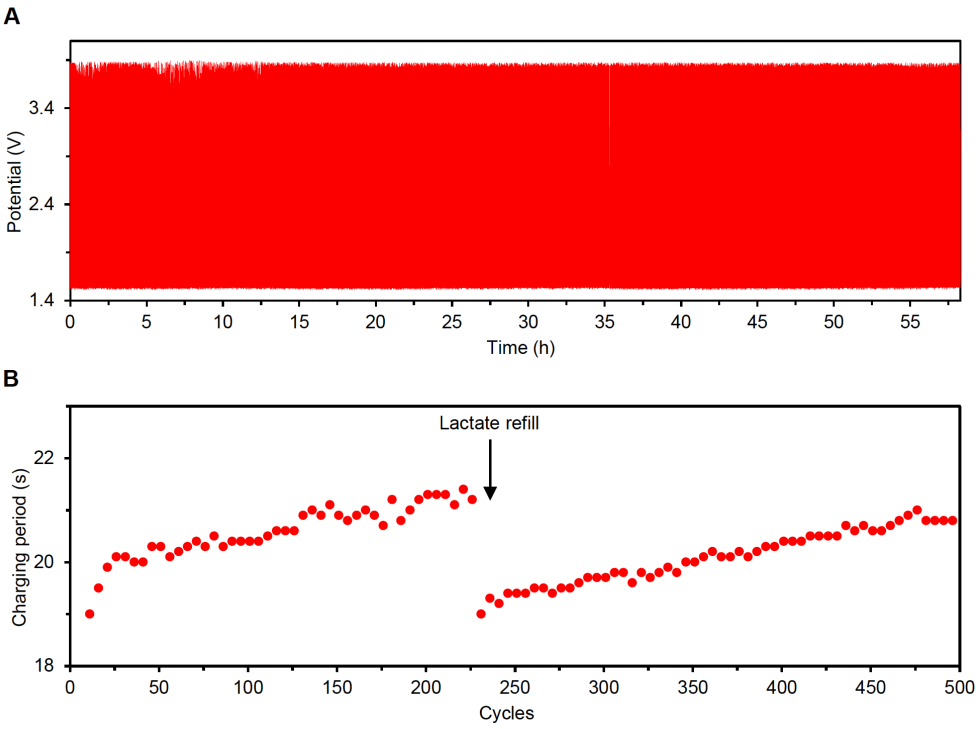

Fig. S19. Long-term stability of the BFCs to charge a capacitor. (**A**) Performance of the BFCs for charging a capacitor (220 μF) for nearly 60 hours in a 20 mM lactate solution. (**B**) The period to charge the capacitor (220 μF) from 1.8 to 3.8 V. Fresh 20 mM lactate fuel was filled after 220th cycle.

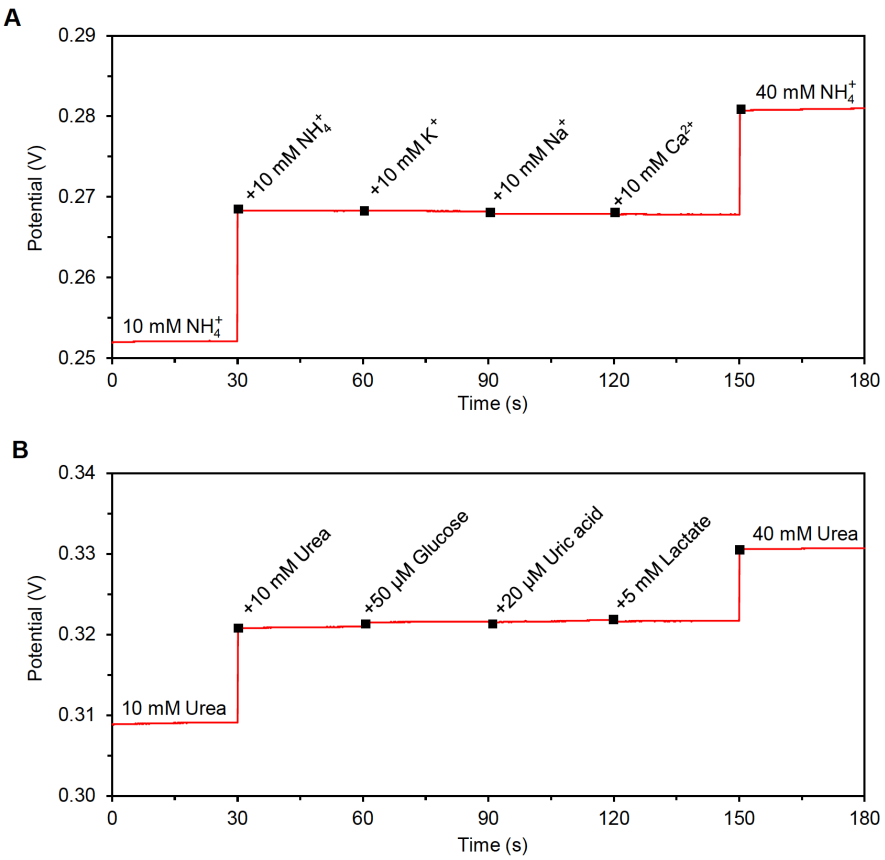

Fig. S20. Selectivity of the sensor arrays. (**A** and **B**) Selectivity of the NH_4^+ (**A**) and urea (**B**) sensors. Data recording was paused for 30 s for each solution change. Experiments were repeated three times independently with similar results.

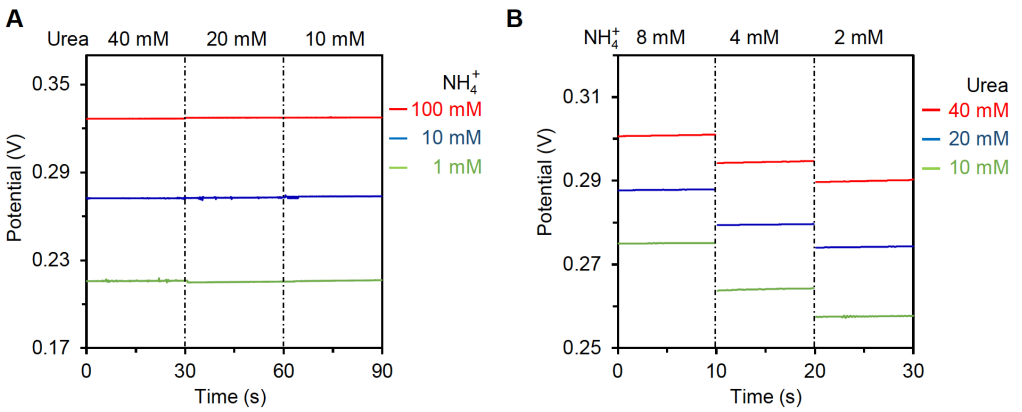

Fig. S21. Interactive study of the urea/NH_4^+ sensor array. (**A** and **B**) OCP curves of an NH_4^+ sensor (**A**) and a urea sensor (**B**) under various concentrations of urea and NH_4^+. Data recording was paused for 30 s for each solution change. Experiments were repeated three times independently with similar results.

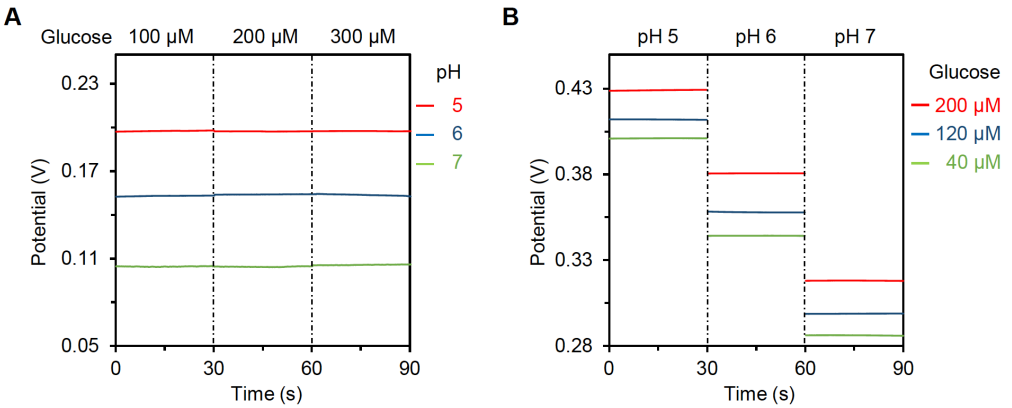

Fig. S22. Interactive study of the glucose/pH sensor array. (**A** and **B**) OCP curves of a pH sensor (**A**) and a glucose sensor (**B**) under various concentrations of glucose and different pHs. Experiments were repeated three times independently with similar results.

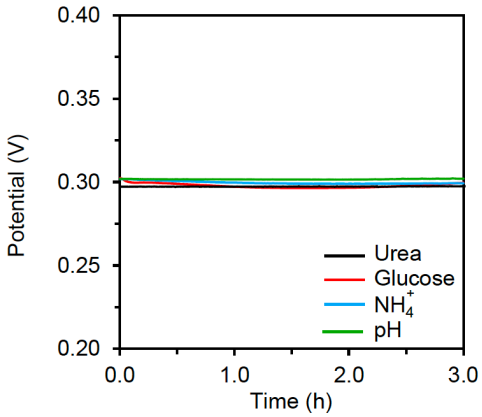

Fig. S23. Stability of the sensor arrays. Long-term stability of the urea (black), glucose (red), NH_4^+ (blue) and pH (green) sensors in 20 mM urea, 100 μM glucose, and 10 mM NH_4^+, respectively. Experiments were repeated three times independently with similar results.

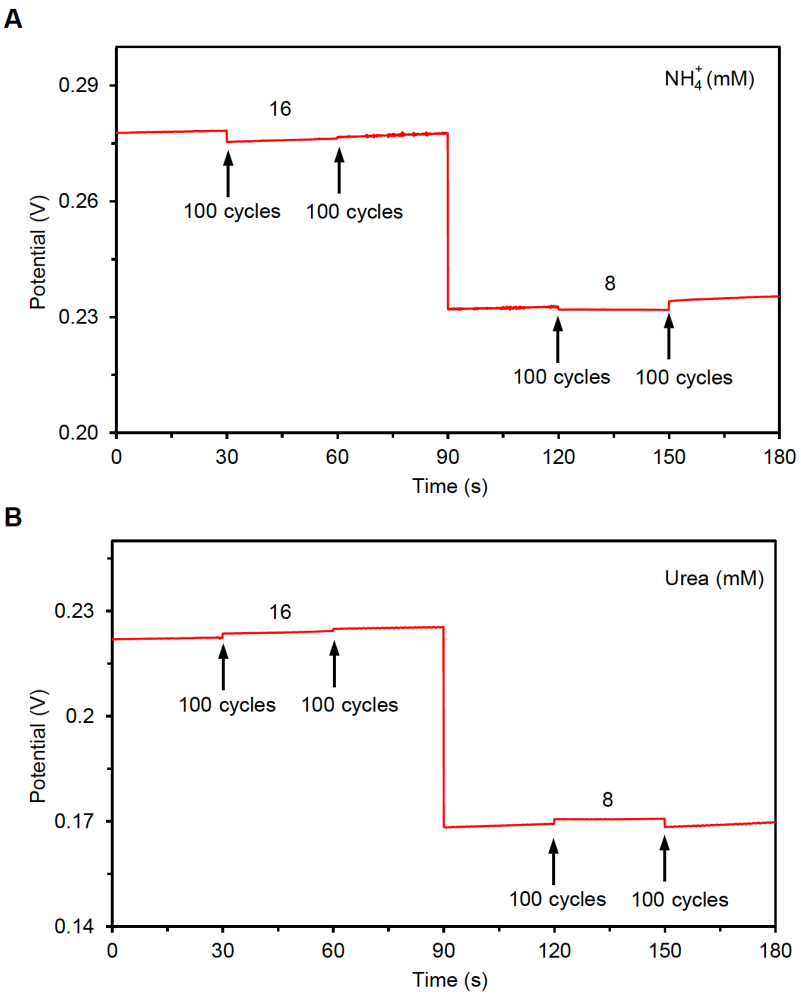

Fig. S24. Performance of the sensor arrays under mechanical deformation. (**A** and **B**) Performance of an NH_4^+ sensor (**A**) and a urea sensor (**B**) after 0, 100 and 200 cycles of bending (radius of bending curvature, 4 cm). Experiments were repeated three times independently with similar results.

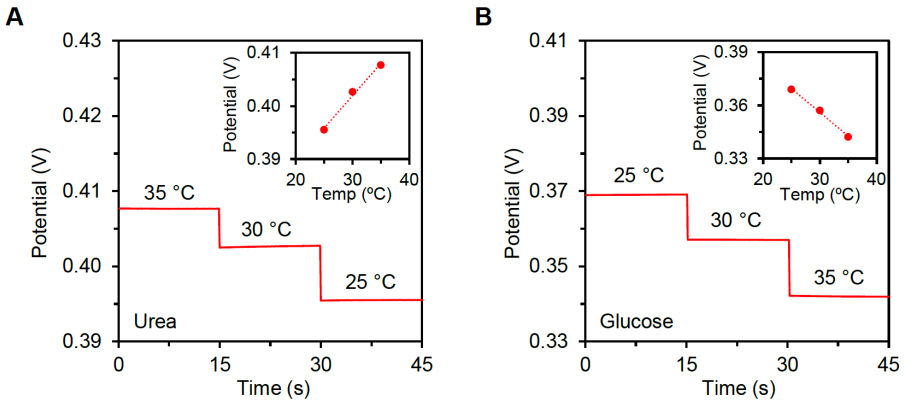

Fig. S25. Influence of the temperature on the performance of enzymatic sensors. (**A** and **B**) OCP responses of a urea sensor (**A**) and a glucose sensor (**B**) under different temperatures in the presence of 10 mM urea and 100 μM glucose, respectively. Insets, the corresponding calibration plots of the glucose and urea sensors under different temperatures. Sensor readings were paused during the temperature change. Experiments were repeated three times independently with similar results.

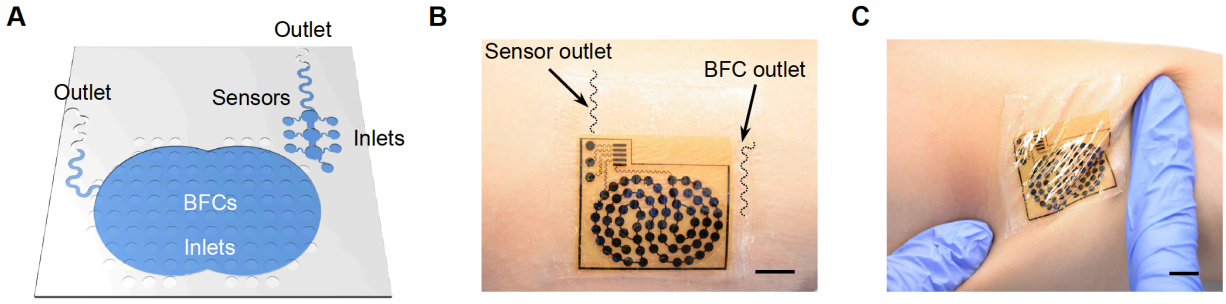

Fig. S26. Skin-interfaced microfluidic patch in the PPES. (**A**) Schematic illustration of the microfluidic design of the PPES. (**B** and **C**) Photographs of a skin-interfaced microfluidic electrochemical patch on a human subject's arm. Scale bars, 1 cm.

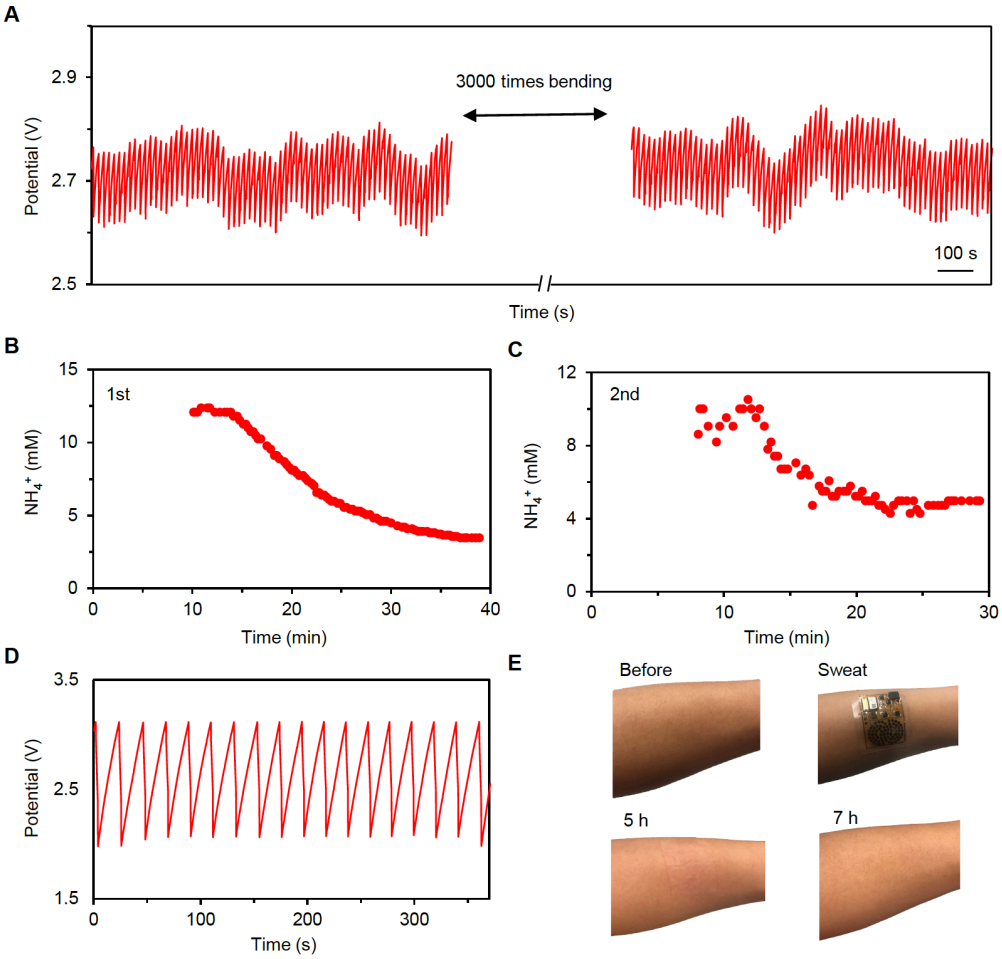

Fig. S27. Investigation of the stability, reusability, and biocompability of the PPES. (**A**) The charging performance of the PPES (680 μF capacitor) in 20 mM lactate before and after 3000 times bending cycles (radius of bending curvature: 1.5 cm). (**B** and **C**) Repeating use of a PPES for sweat NH^{4+} analysis on a subject's forehead during the same day. The PPES patch was peel off from the skin after the first cycling test; 4 hours later, the patch was reattached on the skin for the second cycling test. (**D**) Real-time capacitor potential of the PPES charged by the BFC array in a 20 mM lactate after one-month storage at 4 °C. (**E**) The biocompability test of the PPES. The PPES was worn by a healthy subject for 5 h involving a 40-min cycling exercise in the first hour.

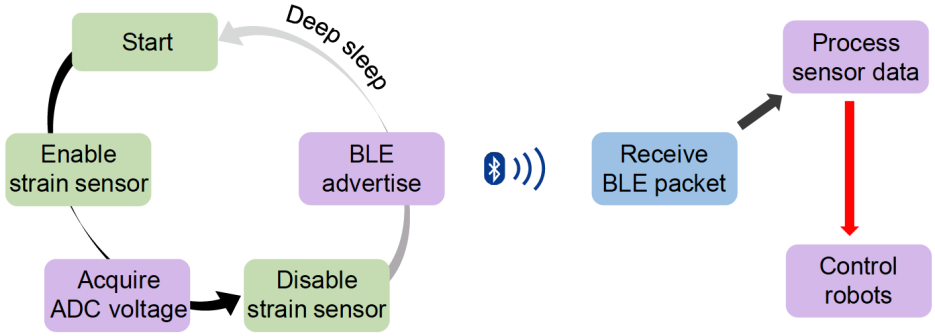

Fig. S28. Operation flow of data transmission processes and human-machine interaction.

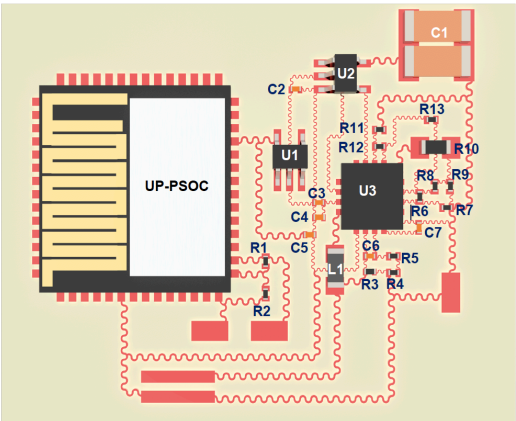

The list of the components

Components	Description	Value and series number
UP-PSOC	EZ-BLE™ Creator Module	CYBLE-214009-00
U1	Voltage Regulators	TPS71721
U2	Analogue Switch	MAX4715EXK+T
U3	Boost Converter	BQ25504
L1	Fixed Inductors	MLZ1608
C1	0402 Capacitor	220 μF*2
C2	0202 Capacitor	0.1 μF
C3	0202 Capacitor	4.7 μF
C4	0202 Capacitor	0.1 μF
C5	0202 Capacitor	0.1 μF
C6	0202 Capacitor	4.7 μF
C7	0202 Capacitor	0.1 μF
R1	0202 Resistor	200 kΩ
R2	0202 Resistor	200 kΩ
R3	0202 Resistor	10 MΩ
R4	0202 Resistor	4.99 MΩ
R5	0202 Resistor	4.99 MΩ
R6	0202 Resistor	4.32 MΩ
R7	0202 Resistor	5.6 MΩ
R8	0202 Resistor	3.6 MΩ
R9	0202 Resistor	6.2 MΩ
R10	0402 Resistor	0 Ω
R11	0202 Resistor	4.02 MΩ
R12	0202 Resistor	3 MΩ
R13	0202 Resistor	3 MΩ

Fig. S29. Schematic illustration and component list of the strain sensor integrated PPES for human-machine interaction.

Text S1. Mechanism of TTF-MDB bimediator in BFC.

TTF and MDB can act as electron-transfer relay systems between bioanode and the flavin adenine dinucleotide (FAD)/FADH (the redox active centers of lactate oxidase protected by the protein shell). Generally, L-lactate is oxidized by the FAD of LOx, generating the reduced form LOx(FADH) as the following process:

$$\text{L-lactate} + \text{LOx(FAD)} \rightarrow \text{pyruvate} + \text{LOx(FADH)} \quad (1)$$

Then, the LOx(FADH) is oxidized by the TTF/MDB mediator:

$$\text{LOx(FADH)} + 2\text{TTF}^{+} \rightarrow \text{LOx(FAD)} + 2\text{TTF} + 2\text{H}^{+} \quad (2)$$

$$2\text{TFF} \rightarrow 2\text{TTF}^{+} + 2\text{e}^{-} \quad (3)$$

$$\text{LOx(FADH)} + \text{MDB}_{red} \rightarrow \text{LOx(FAD)} + \text{MDB}_{ox} + 2\text{H}^{+} \quad (4)$$

$$\text{MDB}_{red} \rightarrow \text{MDB}_{ox} + \text{e}^{-} \quad (5)$$

Electrons transfer from the mediators to the bioelectrode as shown in equation (3) and (5).

Without the additional mediator, the O_2 would be the oxidizer for the reduced LOx(FADH):

$$\text{LOx(FADH)} + \text{O}_2 \rightarrow \text{LOx(FAD)} + \text{H}_2\text{O}_2 \quad (6)$$

At low potential, the electron transfer rate between the generated H_2O_2 and the carbon-based electrode is very low (H_2O_2 oxidation requires a high voltage). Instead, the onset potential of the MDB and TTF are -0.2 and 0 V, respectively (as shown in Fig. 2D). Here, bioanode mixed with TTF and MDB has higher current and lower onset potential than either of single mediator.

Table S1. List of BFCs for energy-harvesting in body fluids.

No.	Bioanode	Cathode	Biofluid	Biofuel	Power output	OCP (V)	Reference
1	Pyranose dehydrogenase/graphite	BOx/AuNPs/Au	Blood	Glucose	73 $\mu W\ cm^{-2}$	0.56	49
2	LDH/buckypaper	BOx/buckypaper	Tear	Lactate	8.14 $\mu W\ cm^{-2}$	0.41	50
3	Cellobiose dehydrogenase/Au NPs/Au	BOx/AuNPs/Au	Sweat	Glucose	0.26 $\mu W\ cm^{-2}$	0.58	51
			Saliva		0.2 $\mu W\ cm^{-2}$	0.56	
			Tear		1 $\mu W\ cm^{-2}$	0.57	52
4	LOx/NQ-CNT	CNT-Ag_2O	Sweat	Lactate	1.1 $mW\ cm^{-2}$	0.5	32
5	CNT/TTF/LOx/chitosan	Platinum black	Sweat	Lactate	44 $\mu W\ cm^{-2}$	0.5 *	34
6	LOx/TTF·TCNQ/CNT	Platinum black	Sweat	Lactate	100 $\mu W\ cm^{-2}$	0.67	53
7	LOx/TTF-MDB-CNT/rGO/h-Ni	Pt-Co/MDB-CNT	Sweat	Lactate	3.5 $mW\ cm^{-2}$	0.65	This work

BOx, bilirubin oxidase; LDH, lactate dehydrogenase; NPs, nanoparticles; NQ, 1,4-naphthoquinone; TCNQ, tetracyanoquinodimethane; OCP, open circuit potential.

Physiological range of the biofuels: Glucose: blood, 4.4-7.8 mM; saliva, 0.02-0.06 mM; tear, 0.2-0.9 mM. Lactate: sweat, 5-60 mM.

*Acquired from provided figure.